Polymer
April 2022, Volume 247, Pages 124757 (8p.)
https://doi.org/10.1016/j.polymer.2022.124757
https://archimer.ifremer.fr/doc/00761/87282/

Correlation between crystallization and mechanical stress reveals by chain scission of segmented amide copolymer

Bardin Antoine [1, 2, 3], Le Gac Pierre Yves [1, *], Albouy Pierre-Antoine [4], Bindi Hervé [2], Fayolle Bruno [3]

[1] Marine Structure Laboratory, IFREMER, Centre de Bretagne, 29280, Plouzané, France
[2] Thales DMS France, 525 Route des Dolines, 06560, Valbonne, France
[3] PIMM Laboratory, Arts et Metiers Institute of Technology, CNRS, Cnam, HESAM Université, 151 Boulevard de l'Hôpital, 75013, Paris, France
[4] Laboratoire de Physique des Solides, UMR 8502, Université Paris-Sud, Université Paris-Saclay, 91405, Orsay, France

* Corresponding author : Pierre Yves Le Gac, email address : pierre.yves.le.gac@ifremer.fr

Abstract :

By tuning hydrolysis duration of a segmented ether-amide copolymer (PEBA), a range of specimens presenting various macromolecular structures has been produced. Knowing that scissions occur predominantly at the bond between hard and soft blocks, for a given hard phase structure we study the impact of phase interconnection changes on strain-induced crystallization (SIC) occurring during tensile loading. The consequences of chain scissions on the structural reorganization involving SIC measured with in situ X-ray diffraction is considered here for the first time. A close correlation between stress and crystallinity induced under strain is highlighted whatever the chain scission number, i.e. the number of phase interconnections. As a result, the stress decrease observed at a given elongation can be interpreted as a consequence of a SIC weakening with the chain scission process.

Graphical abstract

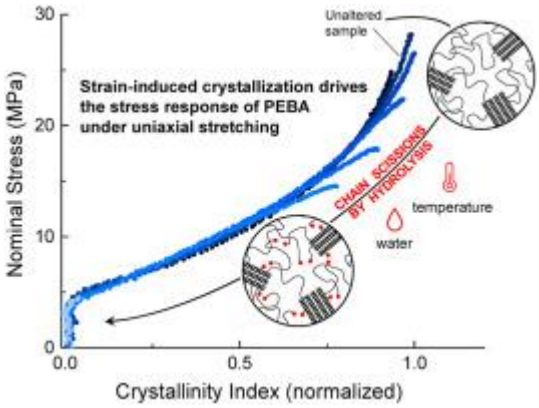

Highlights

► A range of PEBA presenting various macromolecular structures has been produced after hydrolysis. ► Chain scission changes strain-induced crystallization (SIC) occurring during tensile loading. ► A close correlation between stress and crystallinity induced under strain is highlighted.

Keywords : thermoplastic elastomer, Poly(ether-block-amide), PEBA, chain scission, strain-induced crystallization

1. Introduction

Strain-induced crystallization (SIC) is at the origin of the remarkable mechanical properties of many elastomers such as natural polyisoprene [1-5], polychloroprene rubbers [6, 7] or some polyurethane elastomers. It results from the alignment of amorphous molecular chains in the stretching direction, lowering the crystallization entropy cost [8]. In thermoplastic elastomers (TPEs), the crystallization of the soft phase upon stretching is accompanied by a reorganization of the hard domains. These complex morphological transformations have been particularly studied on urethane segmented copolymer (TPU) [9-11] and poly(ether-block-amide) (PEBA) [12-15].

PEBA is composed of alternating flexible soft polyether segments and rigid hard polyamide segments. By modifying the weight ratio or the length of the respective segments, it is possible to tune the physico-chemical properties of the material. Grades can thus exhibit a mechanical behaviour ranging from rubber, for low PA content, to homopolymer-like PA, for high PA content [16, 17]. They exhibit a micro-phase separated morphology, consisting of hard microdomains dispersed throughout a soft phase matrix [18]. Some amorphous PA segments remain isolated into the soft phase, as covalent bonding between both blocks prevent a perfect segregation. In case of soft PEBA grades as considered here, the extent of PA crystallization is limited by the low PA content [15, 17-19].

The PEBA reorganization under stretching has been described in the literature as a three-stage process [19, 20]. Starting from the quiescent state (macroscopic elongation $\lambda = 1$), drawing up to $\lambda = 2$ simply results in an extension of the soft segments. PA lamellae start to rotate at higher draw ratio and become oriented in a tilted direction with respect to the draw axis (observation of a cross-like SAXS pattern [20]). Lamellae start to break at around $\lambda = 4$, leading to the formation of fibrils oriented in the tensile direction. It also induces some relaxation of the soft polyether segments, from thereon orienting at a lower rate with

increasing elongation [19]. This progressive lamellae break-up, moderate soft chains orientation and crystallization, proceed up to high elongation.

This study is part of a project investigating the ageing behaviour of thermoplastic elastomers in marine environment [21 - 23]. The immersion of samples in natural seawater leads to hydrolysis, resulting in molecular chain scissions. We used this framework as an opportunity to study the strain-induced crystallization of PEBA through a novel approach. Indeed, a common approach for TPEs is to compare grades with different hard/soft ratios [13, 15, 17, 19]. However, many parameters are affected by this ratio, such as soft segment length, crystalline domain size or the global organization of the material. This method is then not best suited to separate the respective contribution of each parameter. More recently, the effect of crosslinking networks on SIC has been studied in PTMO [24]: crosslinking has a weak effect on the onset of SIC itself but it promotes the extend of crystallization during deformation. By inducing chain scission through hydrolysis, our approach enables us to produce samples with an essentially preserved structure where the only changing parameter is the degree of connections between the soft and hard blocks associated with the chain scission number generated by hydrolysis.

According to this approach, we propose here to study the SIC process for samples submitted to different degrees of hydrolysis. The macromolecular, structural, and mechanical changes induced by chain scissions and stretching are presented and discussed here with the aim to propose a new relationship between strain-induced crystallization and mechanical properties.

2. Experimental section

2.1. Materials

The Pebax® 2533 grade was purchased from Arkema in granular form. The specific 2533 SD 02 grade has been selected due to the incorporation of specific stabilizers that prevent oxidation. It ensures that degradation is essentially due to hydrolysis and not oxidation during water aging. Granules were dried at 80 °C for 15 h before processing. Injection of 2.5 mm-thick plates was performed according to supplier specifications on a DK CODIM 175/410 injection molding machine. The Pebax® chemical structure and composition are recalled in Figure 1. The number of repeating units of soft and hard blocks (n and m respectively), the degree of polymerization N and the different number average molar masses are averaged from data found in the literature on Pebax® 2533 [25-27]. The total molar mass is about 55 000 g.mol^{-1} and the polyamide weight ratio is 23 %.

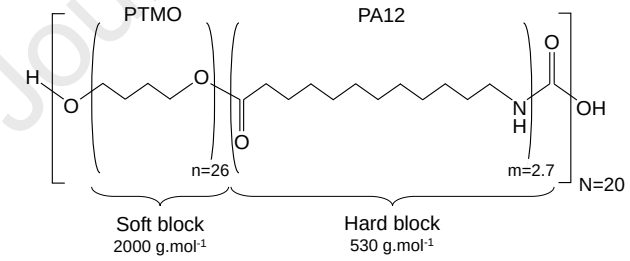

Figure 1. Pebax® 2533 chemical structure and composition.

2.2. Hydrolysis conditions

Before starting the chemical degradation process, plates were annealed at 110°C for 15 h under vacuum to stabilize the microstructure. Slow cooling to ambient was simply obtained by turning off the oven.

Differential scanning calorimetry analysis (not shown here) confirmed a stable microstructure (no additional melting peak) up to 110 °C. Samples were then immersed in tanks filled with continuously renewed natural seawater at four temperatures: 40, 60, 80, and 90 ± 2 °C. They were removed from the tanks after a definite time and carefully wiped with a paper towel. To avoid further hydrolysis, samples were fully dried in a desiccator filled with silica gel (i.e., RH close to 0) at 40 °C for 48 h prior to testing. A special attention was paid to ageing conditions and sample geometry to ensure that the samples were hydrolyzed homogenously through the thickness, in others words to ensure that water diffusion was much faster than hydrolysis kinetics. In fact, considering water diffusion in Pebax at 80°C, a typical Fickian behavior is observed with a time to reach saturation within the material about 0,1 day. In the meantime, it can be seen that the amount of chain scission after 7 days at 80°C is very low (about 0,01mol/kg). It means that de water diffusion is much faster than the hydrolysis rate (at least by a factor of 10) and so degradation is homogeneous through thickness during ageing. The same behavior is observed for all ageing temperature.

Finally, it is noteworthy that characterizations were performed with dried samples, to be in the same state for all tests (i.e. tensile tests, DSC, X Ray, GPC). Tensile tests have been performed with and without drying, no major changes in mechanical behavior were observed.

2.3. Chain scission measurement

Molar mass was measured with gel permeation chromatography by the PeakExpert Company. Analyses were performed at 20 °C using a mixture of hexafluoroisopropanol and 0.1 M potassium trifluoroacetate as eluent. The apparatus was equipped with a pre-column and two columns packed with 7 μm PFG particles of 1000 Å and 100 Å pore size, respectively. The detection was performed using a

Waters 2414 differential refractive index detector. The calibration was performed with poly(methyl methacrylate) samples.

2.4. Conventional tensile test

Uniaxial tensile tests were performed at a rate of 50 mm/min on a 10 kN capacity Instron machine in a room regulated at 21 ± 1 °C and 50 % relative humidity. A 500 N load cell was used. Dogbone samples were cut according to ISO 37:2005 type 3 (50 mm overall length, 2.5 mm thickness) and two duct tape marks were placed at the gauge length, 15 mm apart. A camera coupled to a specific software developed at IFREMER allows the relative displacement of the two tape markers to be tracked. The tensile modulus (*E*) was estimated from the initial slope of the stress-strain curve.

2.5. Static Small and Wide X-Ray Scattering (SAXS and WAXS)

SAXS and WAXS analysis were performed without any mechanical load applied on the high brilliance SWING beamline at the Soleil Synchrotron facility. A wavelength λ_{XR} = 0.0775 nm is selected by thee monochromator. Patterns were recorded at room temperature, with a CCD detector located at 6 m from the sample for SAXS, and 0.5 m for WAXS. 1D curves were obtained by circular averaging of 2D patterns, using the Foxtrot software. Thanks to the fast processing here, 10 images are collected for the same position of a sample. Resulting WAXS and SAXS curves are respectively plotted as function of the scattering angle 2θ and the wave vector q, with $q = 4\pi.\sin(\theta)/\lambda_{XR}$. The long period L corresponding to the diffraction peak observed in SAXS was calculated as $L = 2\pi/q$, considering the Lorentz correction. Fityk software was used for signal treatment, enabling a crystallinity index to be determined as the ratio of peak area attributed to Bragg diffraction to the signal total area.

2.6. In situ X-ray diffraction under mechanical load

Tests were performed on a symmetric tensile device mounted on a rotating anode X-ray generator (focus size: 0.2 × 0.2 mm^2; 40 kV, 40 mA) equipped with a copper anode whose K_α radiation (wavelength 0.1542 nm) is selected by a doubly curved graphite monochromator [28]. The sample is located at the focalization point close to the collimator exit, which ensures maximum diffracted intensity. Diffraction patterns are recorded with an indirect illumination CCD camera. A beam-stop is fixed close to the camera and contains a photodiode that delivers a photocurrent proportional to the X-ray intensity transmitted through the sample. The exposure time was set at 10 s. An optical camera was used to measure elongation, following the same method as for conventional tensile tests (section 2.4). ISO 37:2005 Type 2 dogbone tensile samples were tested (75 mm overall length, 2.5 mm thickness), at a rate of 10 mm/min, at 20 °C. A detailed description of the apparatus used here can be found in [1-7].

2.7. In situ X-ray data processing

Relevant data are retrieved from two angular scans, one centered on the equatorial Bragg lobes forming upon stretching, the other centered more inwards to only include diffraction by the pure amorphous phase (Figure 2). This procedure enables to separate the respective contributions of the crystalline and amorphous phases. 1D azimuthal profile corresponding to each scan was obtained by radially integrating the signal between the 2θ bounds of the scan area, for $-80° < \varphi < 80°$.

The azimuthal profile of the pure amorphous phase (containing the PTMO and some amorphous PA blocks not contributing to the crystalline phase) was fitted with a $A + B \cos^2 \varphi$ function, following the Gaussian theory of rubber elasticity. The associated Legendre coefficient $\langle P_2^{RX} \rangle = (3\langle \cos^2 \rangle \varphi + 1)/2$ is assumed to be proportional to the Herman coefficient $\langle P_2 \rangle$ for the segmental orientation function of the molten polymer chains. It is recalled that $\langle P_2 \rangle = (\lambda^2 - 1/\lambda)/5N$ within the framework of the Gaussian

model, where λ is the draw ratio and N is the average number of freely jointed statistical segments per chain.

A crystallinity index (CI) was determined by fitting the Bragg peak observed in the first azimuthal profile with a Pearson VII function; the amorphous contribution was accounted for by a square cosine function similar to what is done with the inner angular scan. Indeed, the outer scan captures most of the diffracted intensity and the ratio of Pearson VII function surface by the total integrated intensity is expected to be close to the crystallinity. To avoid any ambiguity this CI was normalized by setting to unity its maximum value, all samples considered (it corresponds to the sample with scissions = 0.6×10^{-2} $mol.kg^{-1}$).

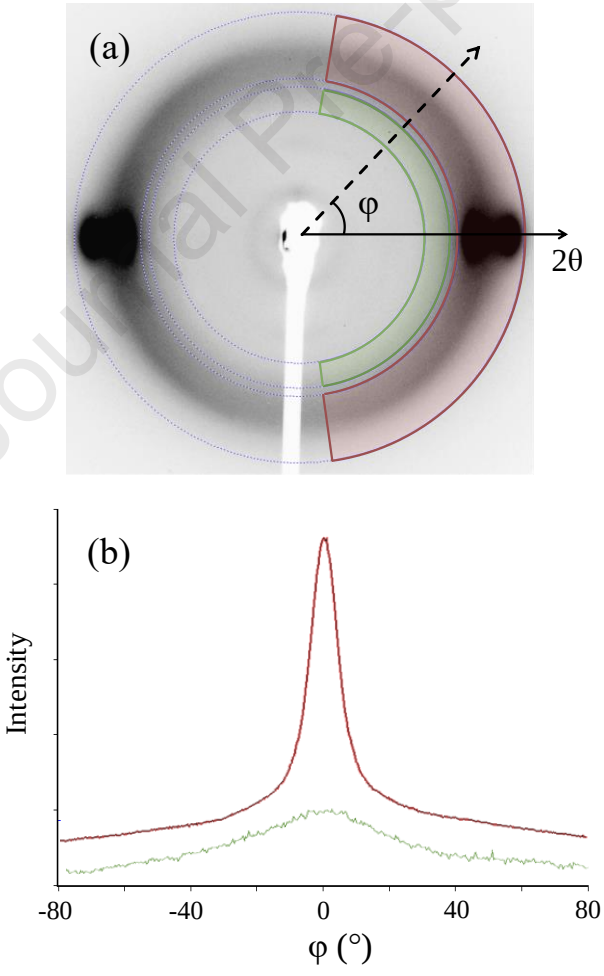

Figure 2. (a) Diffraction pattern of a stretched sample with the two integration areas, one including the diffraction lobes and the other including a pure amorphous phase. In (b) the corresponding diffractograms are plotted, resulting from the radial integration in the respective areas.

3. Results and discussion

3.1. Chain scission process

A chain scission process was induced by hydrolysis to produce a range of poly(ether-block-amide) (PEBA) samples with various macromolecular structures. The mechanism responsible for the chain scission process is discussed later. Scission directly affects the average molar mass, and this last was measured with GPC so as to estimate the chain scissions concentration. This last parameter is calculated according to: $Scissions = \frac{1}{M_n(t)} - \frac{1}{M_{n0}}$ where M_{n0} is the initial average molar mass and $M_n(t)$ its value after immersion time t. Samples were immerged at different temperatures from 40 to 90 °C, for up to 700 days. The chain scission kinetics occurring in the PEBA are reported in Figure 3 and a clear effect of the ageing temperature on the scission kinetics is actually observed. Results for scissions up to 7×10^{-2} mol.kg^{-1} are shown here, but an important brittleness is already observed for scission contents above 4×10^{-2} mol.kg^{-1}. Further observations will thus be limited to this maximum value. Finally, polydispersity remains unchanged for all ageing conditions and close to 2 (data not shown).

Regarding the degradation mechanism, two sites are particularly susceptible to hydrolysis in PEBA: the amide group in the hard segment and the ester group located at the junction of hard and soft segments. This ester group results from the polycondensation of alcohol-terminated PA block and acid-terminated PTMO block. Since the ether segment of PTMO is known to be much less sensitive [29], hydrolysis is expected to occur at the amide or ester sites. To identify the weakest group, a homopolymer PA12, which constitutes the PEBA's hard segments, was also immerged at 80 °C for comparison. In Figure 3 we can see that, at 80 °C, the PA12 chain scissions rate is significantly lower than observed for the PEBA. As this grade only contains 23 $\%_w$ of PA hard segments, we can conclude here that scissions marginally occur in the hard segments. The ester group is consequently the primary site of hydrolysis. This

observation is consistent with other hydrolytic degradation studies of poly(ester-amide) segmented copolymers [30, 31].

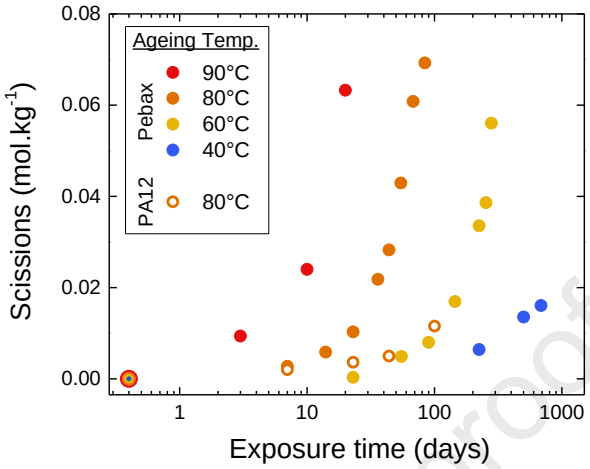

Figure 3. Chain scission kinetics of the PEBA and the PA12 homopolymer constituting PEBA's hard segments aged at different temperatures in water.

3.2. Undeformed PEBA microstructure

To investigate potential morphological changes induced by chain scissions, SAXS and WAXS measurements were performed in the undeformed state (no mechanical load applied) for the PEBA samples presenting increasing chain scission concentrations (Figure 4). Both SAXS and WAXS results show that there is no major impact of the chain scission process on the morphology of the PEBA. Nevertheless, if we look at the results in detail, the following comments can be made:

i) The initial WAXS diffractogram (Figure 4-a) shows a large broad peak, characteristic of a predominant amorphous organization. The small broad peaks at shorter ranges (7.9 and 16.8 Å) are related to the well-ordered PA12 domains, and more precisely to a long-range order of amide groups along the chain [32 - 34]. For low degradation level, i.e. when scissions equal to 2.2×10^{-2} mol.kg^{-1}, we observe a peak growing at 4.2 Å, that corresponds to the γ-

crystalline phase of PA12 [32-34]. From 2.8×10^{-2} mol.kg^{-1} on, the soft segment crystallization is evidenced by two peaks growing at 3.7 and 4.5 Å that are related to the thermal crystallization of PTMO [35]. This means that the PTMO crystalline phase is stabilized by chain scissions. However, this stabilization occurs at a degree of scissions where the PEBA has lost most of its initial mechanical properties (see Figure 5 and Figure 6). PTMO crystallization can explain the embrittlement of PEBA at a high level of degradation but is not involved in the changes of the strain induced crystallization process that will be highlighted later on.

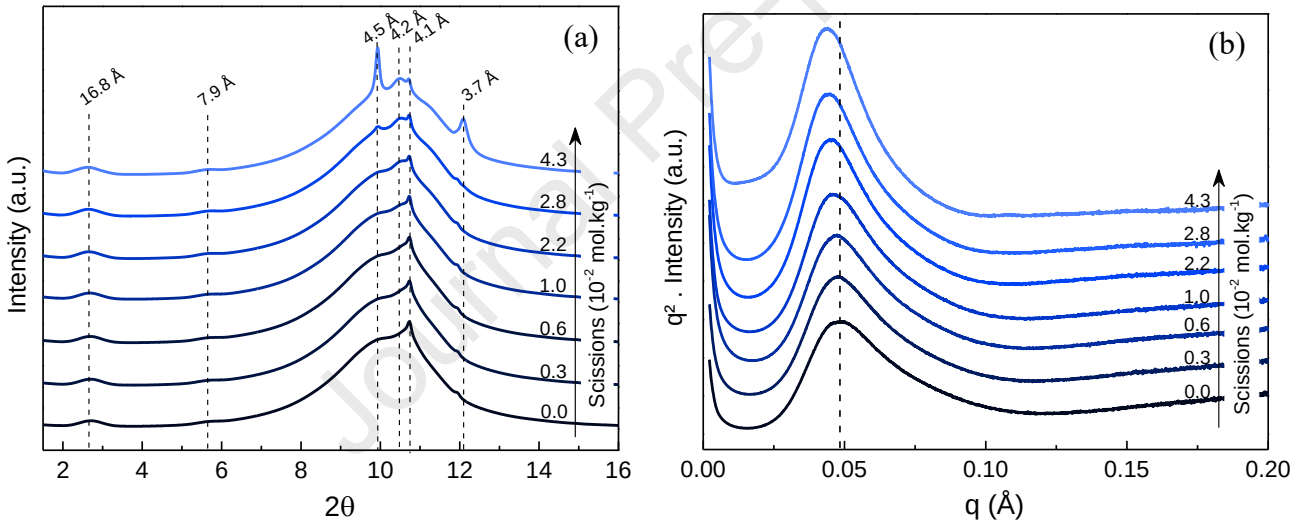

Figure 4. Effect of chain scissions on the PEBA morphology: (a) WAXS and (b) SAXS diffractograms resulting from measurements in the quiescent state (no mechanical load applied) at room temperature.

ii) SAXS data corrected for the Lorentz factor q^2 are plotted in Figure 4-b. A broad peak is observed, characteristic of some stacking order: it may be associated to the PA inter-lamellar order [20]. The corresponding long period *L*, calculated from the position of the peak maximum, is initially ca.13 nm, consistent with data reported in the literature for similar PEBA grades [14-20]. A slight peak shift towards lower q-values is observed at high scission

degrees, reflecting an increase of the long period by about 10 %. This 10% increase during chain scission is considered minor in comparison with the increase of L that occurs during stretching; for example, a 100 % increase is observed by stretching at $\lambda = 2$ [20].

Overall, we consider here that the PEBA morphology in the undeformed state remains unchanged for scissions less than 4.3×10^{-2} mol.kg^{-1}, for higher degradation levels differences can be observed but the material is brittle and cannot be stretched anymore. Let us now focus on changes in the strain induced crystallization process in the following sections.

3.3. Mechanical behaviour

In what follows, the tensile modulus E is defined by the initial slope of the stress-strain curve. Its dependence upon scission concentration is reported in Figure 5. We see that E decreases almost linearly up to a concentration 4.3×10^{-2} mol.kg^{-1}. The data obtained at different ageing temperatures superpose well, forming a master curve, even though the scission kinetics are greatly affected by temperature (as seen in Figure 3). Although a correlation between scissions and modulus can be assumed according to rubber theory, this point will not be further investigated here since chain scissions cannot rigorously be considered as random in the soft phase. Moreover, hydrolysis can also create new physical crosslinking or modify the entanglement density within the polymer leading to complex interpretation of results presented in Figure 5.

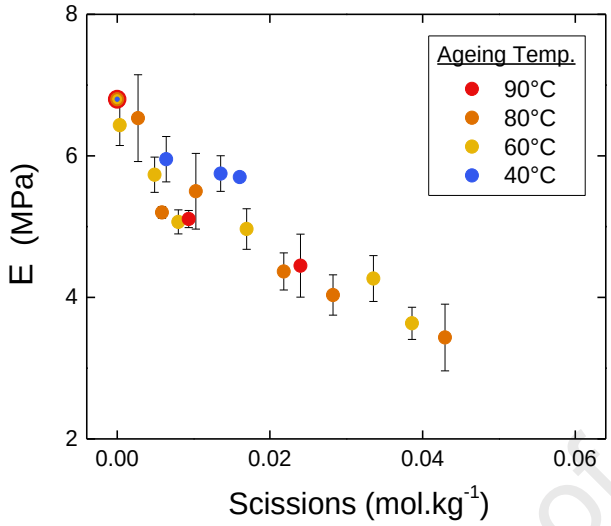

Figure 5. Change in the PEBA modulus with chain scissions induced by hydrolysis. The tensile modulus E is defined as the slope for $1 < \lambda < 1.2$.

The data for the nominal stress at break σ_b and elongation at break λ_b also exhibit master curves whatever the chain scission kinetics (Figure 6). λ_b presents at first a slight increase and a plateau, followed by a drop (Figure 6-b). On the other hand, the global λ_b behaviour is similar to what is observed in conventional linear thermoplastic polymers where fracture properties remain constant above a specific molar mass M_n and sharply drop below that value. A critical molar mass M'_c, related to the ability of the amorphous chains to form entanglements is thus identified. The relationships between fracture properties and molar mass of segmented urethane and amide copolymers have been addressed in detail in a previous publication [23]. We see in Figure 6-b that σ_b decreases almost linearly with scissions. This point is discussed below, in regard of the SIC contribution to the nominal stress upon stretching.

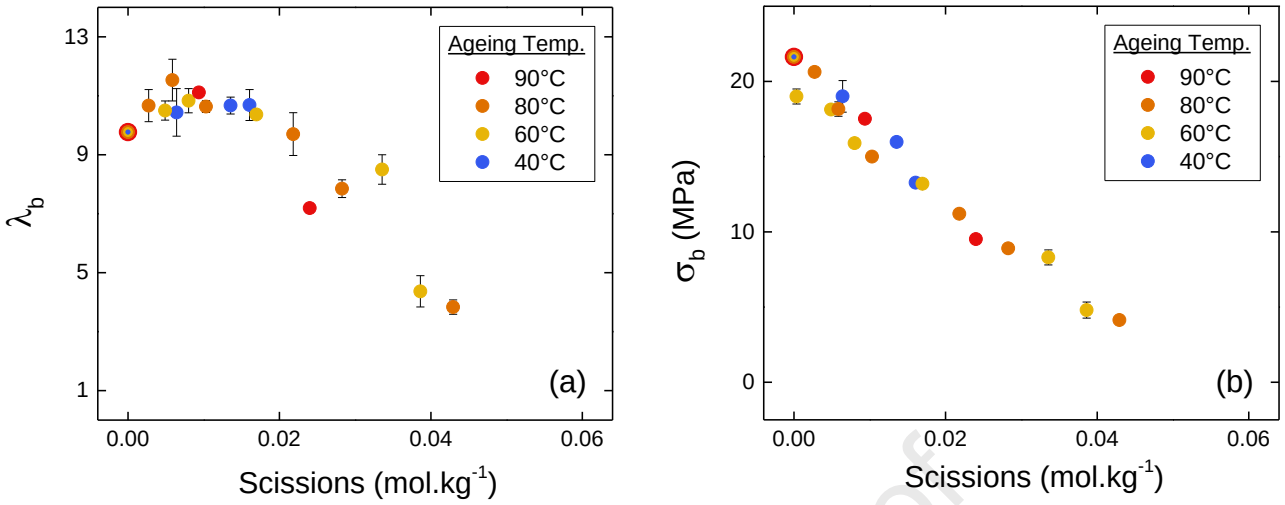

Figure 6. Effect of chain scissions induced by immersion at different temperatures on the PEBA's (a) elongation at break and (b) nominal stress at break.

3.4. Strain-induced morphological change

In situ X-ray diffraction measurements were performed to investigate the morphological changes occurring in PEBA upon stretching up to break. For the sake of clarity, the patterns are displayed with two different levels of contrast (upper and lower rows). The corresponding tensile curve is presented in Figure 8. In the undeformed state, a broad halo is observed, characteristic of an isotropic amorphous organization. On the low brightness image (lower row), we can discern two inner rings, corresponding to lower 2θ, related to the long-range order of PA segments (visible at 7.9 and 16.8 Å in Figure 4) [36]. On the high brightness shot (upper row), a thin, intense ring can be discerned on the outer part of the amorphous halo, corresponding to the 4.1 Å Bragg peak previously observed. Overall, the in-situ X-ray patterns for $\lambda = 1$ are consistent with static XRD analyses.

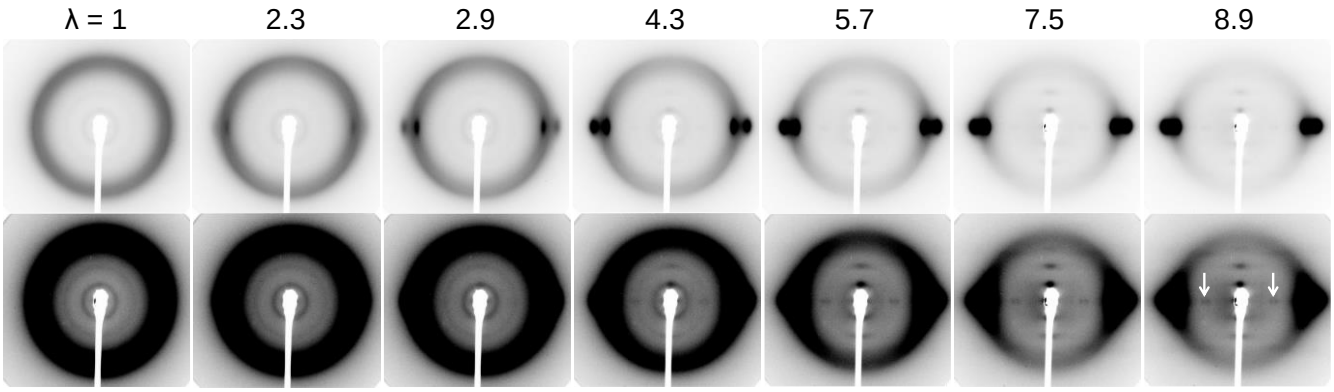

Figure 7. In situ WAXS patterns of a PEBA sample under uniaxial tension (draw direction is vertical). The sample subjected to 1.0×10^{-2} mol.kg^{-1} scissions induced by immersion at 80 °C was here arbitrarily chosen as representative. For the sake of clarity, the patterns are displayed with two different levels of contrast (upper and lower rows). The corresponding tensile curve is presented in Figure 8. Spots indicated with arrows (visible for $\lambda \geq 4.3$) are experiment artefacts, not related to any morphological feature.

As PTMO chains orient in the stretching direction, the amorphous halo gradually concentrates in the equatorial direction, due to inter-chain positional correlations. From $\lambda = 1.7$ on, two well-defined spots become visible in equatorial position and continuously grow in intensity. The angular positions of these spots correspond to the d-spacings of the diffraction peaks of thermally grown PTMO crystallites (3.7 and 4.5 Å, see Figure 4). The two inner rings, associated to the long-range order along the PA chains, concentrate in azimuthal position to form intense spots clearly visible above $\lambda = 2.9$. This was linked to scattering by PA fibrils that results from lamellae breaking [20]. These spots grow in intensity, which reflects the increasing number of fibrils as stretching proceeds.

As detailed in section 2.7, the two relevant parameters that can be derived from the diffraction patterns are a PTMO normalized crystallinity index CI_{norm} and the amorphous phase orientation parameter $\langle P_2^{RX} \rangle$. Let us recall here that CI_{norm} values are normalized with respect to the maximum measured value when

considering all samples (sample with Scissions = 0.6 × 10^{-2} mol.kg^{-1}., see experimental part). $\langle P_2^{RX} \rangle$, CI_{norm} and the engineering stress are plotted in Figure 8 as a function of the draw ratio for a sample with a scission concentration 1.0 × 10^{-2} mol.kg^{-1}, and an ageing temperature 80°C. The $\langle P_2^{RX} \rangle$ increase reflects the progressive alignment of the soft segments along the draw direction. The orientation rate diminishes above λ = 2.5, that corresponds to the point where lamellae start to breakup. The onset of PTMO strain-induced crystallization matches with the upturn in stress, demonstrating its reinforcing effect. All parameters increase steadily up to λ = 6, as PA lamellae progressively break up and soft PTMO segments orientate and crystallize, leading to the PEBA strengthening. Interestingly, above λ = 6, the CI exhibits a plateau, suggesting that SIC has reached a saturation or an equilibrium, even though the soft segments still orientate up to break, as evidenced by the continuous $\langle P_2^{RX} \rangle$ increase. To our knowledge, this phenomenon was not previously reported, possibly since most studies were confined to low to medium deformations.

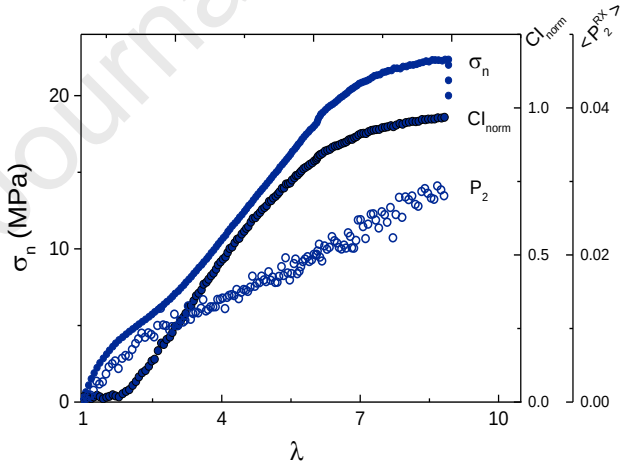

Figure 8. Mechanical and structural changes under stretch of the PEBA sample presenting 1.0 × 10^{-2} mol.kg^{-1} scissions induced by immersion at 80 °C (sample arbitrarily chosen as representative). The nominal stress σ_n, the normalized crystallinity index CI_{norm}, and the amorphous phase orientation parameter $\langle P_2^{RX} \rangle$ are superimposed to highlight structural changes along with their impact on the mechanical behaviour of the PEBA. Corresponding in situ WAXS patterns from which CI_{norm} and $\langle P_2^{RX} \rangle$

are determined are presented in

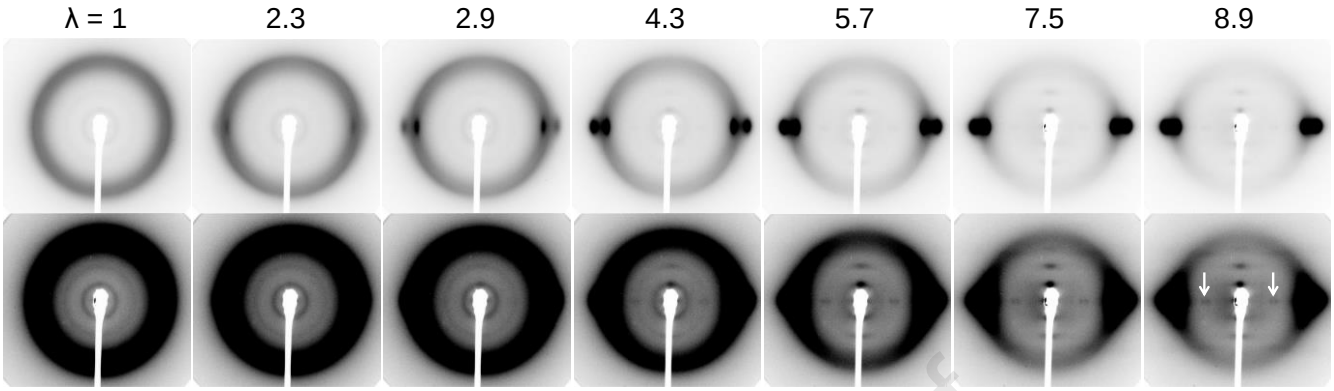

Figure **7**.

3.5. Effect of scissions on the SIC process and mechanical behaviour

The scissions have a dramatic effect on tensile properties (Figure 9), already described in section 3.1. We bring to the reader's attention that the results presented in section 3.1 come from conventional uniaxial tensile tests, while data in Figure 9 come from in situ XRD combined with tensile testing. All crystallinity curves present a sigmoidal shape (Figure 9). For a given elongation, CI decreases with increasing scissions. At high scission levels (4.3×10^{-2} mol.kg $^{-1}$), the SIC is significantly reduced, and mechanical properties dramatically drop. The SIC onset, determined as the intersection of the x-axis with the CI-λ linear fit for CI between 0.1 and 0.5, increases with scissions. A slow-down in crystallization kinetics seems common to all samples and $CI_{norm} = 1$ seems to be close to a plateau value. Further treatment enabled us to estimate that this crystallinity index corresponds to a PTMO crystallinity index of 40 %.

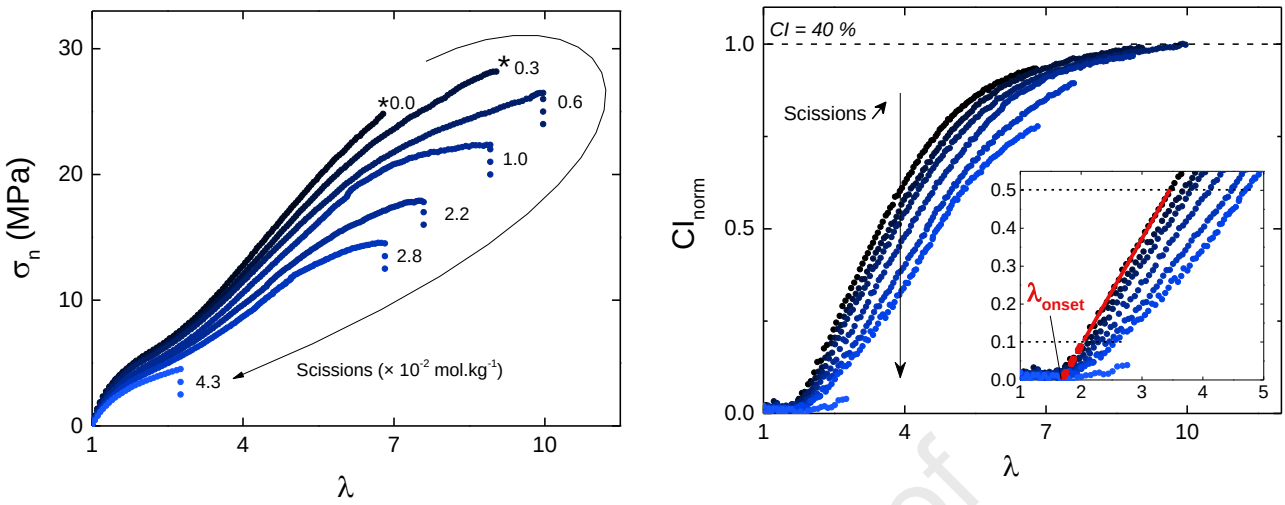

Figure 9. Effect of scissions induced by immersion at 80 °C on the stress and crystallinity of the PEBA. Stars (*) on the σ_n-λ curves indicate that failure was not reached for samples subjected to none and 0.3 × 10^{-2} mol.kg $^{-1}$ scissions, due to slippage of the specimen out of clamps. All crystallinity index data were normalized to the highest CI value reached; all samples considered. The SIC onset was determined as the intersection of the x-axis with the CI_{norm}-λ curve linear fit for $0.1 < CI_{norm} < 0.5$.

Following a common approach used for thermoset elastomers, $\langle P_2^{RX} \rangle$ is plotted as function of $(\lambda^2 - \lambda^{-1})$ (Figure 10). According to the theory of rubber elasticity, the slope, determined between $\lambda = 1$ and the SIC onset elongation, is directly linked to the crosslink density of these materials. Though the PEBA morphology differs from thermoset elastomers, we can consider that the PA hard domains, where PTMO amorphous chains interconnect, may be viewed as mechanically similar to crosslinks in rubbers (TPEs are frequently described as physically crosslinked elastomers). Besides, we previously showed in section 3.4 that, at low strain, the PA crystalline domains do not undergo any major morphological change upon stretching. The $\langle P_2^{RX} \rangle$ slope decrease observed in Figure 10 was caused by scissions occurring between

hard and soft segments (section 3.1). These scissions globally lead to a decrease in the interconnections between hard and soft phases.

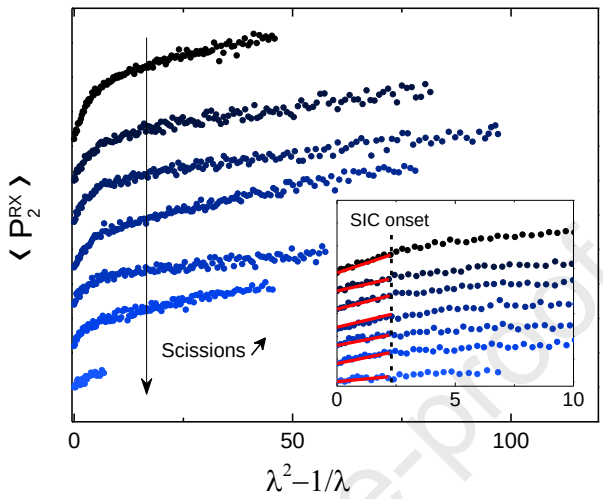

Figure 10. Effect of scissions induced by immersion at 80 °C on the soft segment orientation behavior of the PEBA. The $\langle P_2^{RX} \rangle$ slope was determined for $1 < \lambda < \lambda_{onset\text{-}min}$, $\lambda_{onset\text{-}min}$ being the smallest λ_{onset} measured (all samples considered).

We have also shown in Figure 9 that the crystallinity index measured at a given elongation between the SIC onset and the high-strain CI plateau, decreases with increasing scissions. This can be illustrated by considering the elongation necessary to reach a specific crystallinity index, arbitrarily chosen as CI = 0.5 in the present case (Figure 11). It is interesting to note that this elongation is significantly more sensitive to scissions than λ_{onset} (slope of 2.8 against 0.8). The fact that the crosslinking density influences slightly λ_{onset} has already been shown in the literature [24, 37]. We can then deduce that the increased elongation required to reach CI_{norm} = 0.5 is not only due to the λ_{onset} increase. In other terms, while scissions cause a SIC onset delay, they also affect the ability of the PTMO segments to crystallize at a given elongation. This is illustrated by a slope decrease of the central part of the *CI*-λ sigmoidal curve (Figure 9). Consequently, with increasing scissions, a higher strain is required to reach a given

crystallinity. A possible interpretation is that the chains that underwent scission, being now pendant or free, are not mechanically active anymore, and thus do not stretch. Consequently, they do not contribute to the SIC.

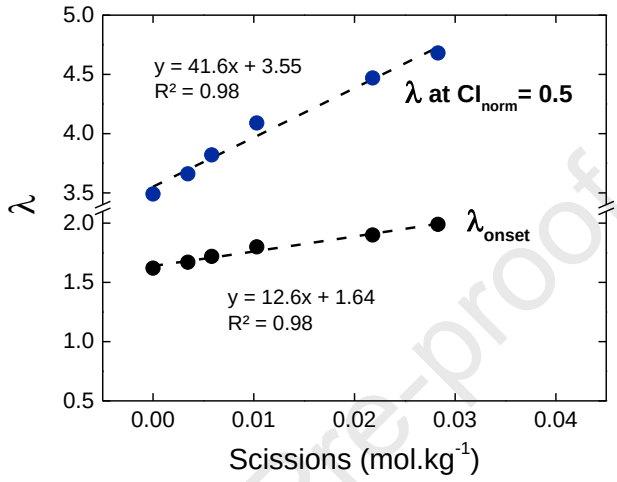

Figure 11. Effect of chain scission, on the strain-induced crystallization onset and on the elongation required to reach a normalized crystallinity index of 0.5. Data presented here correspond to samples immersed at 80 °C.

3.6. SIC contribution to the stress

SIC is known to reinforce elastomers and increase their properties at break, hindering fracture propagation. Though this phenomenon is commonly admitted, it is complicated to actually evaluate the crystallites contribution to the mechanical behaviour. In an attempt to address this point, the stress was plotted as a function of the crystallinity index, for all samples (Figure 12). All curves accurately overlap up to $CI_{norm} = 0.7$, whatever the degree of scissions. At first, the stress value increases without any change in crystallinity, as the low strain behaviour is driven by the amorphous phase (stretching of the soft segments). Once SIC initiates, a steady stress increase is observed with increasing CI. This remarkable

correlation between stress and crystallinity demonstrates that the strain-induced crystallization of the soft segments is the primary phenomenon driving the stress response of the PEBA under uniaxial tension. The stress decrease observed with increasing scissions at a given elongation (Figure 9) then results from a weakening of the SIC.

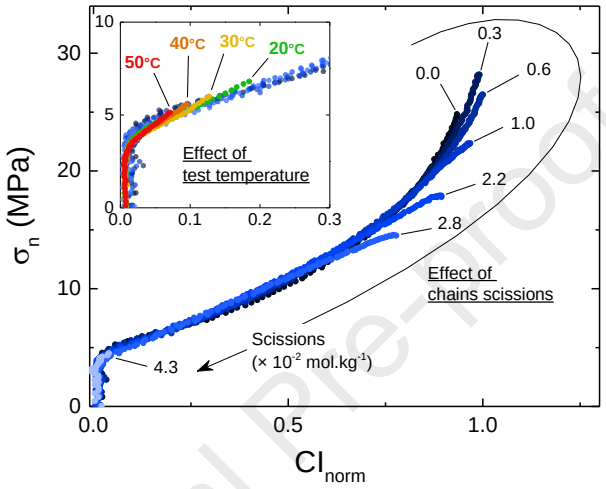

Figure 12. Master curve between nominal stress and normalized crystallinity index of the PEBA presenting varying scission levels induced by immersion at 80 °C. Unaltered samples (not subjected to any scissions) were also tested at different temperatures.

To further test this relationship, another parameter than chain scissions was considered: the testing temperature. In situ XRD tests upon stretching were performed at different temperatures, from 20 to 50 °C, on unaltered PEBA samples. Increasing the temperature significantly affects the SIC phenomenon, increasing the energy barrier that SIC needs to overcome in order to occur. Though the temperature significantly influences the mechanical behaviour and the PTMO crystallization upon stretching, the corresponding *σ-CI* curves overlap with the results obtained from varying the chain scissions (Figure 12). This strengthens our observation: whatever the degree of scissions or the testing

temperature, and even though both parameters greatly affect mechanical and SIC behaviors, a strong correlation is found between stress and crystallinity content.

Conclusions are less straightforward regarding the stress at break (reported in Figure 6 for conventional tensile testing). At high elongation (or high CI), another phenomenon seems to overtake the SIC contribution, resulting in the curve discrepancy from CI_{norm} = 0.7 in Figure 12. This phenomenon is scissions-dependent, as it is the most substantial for the unaltered sample, and then decreases with increasing scissions. At high elongation, the CI was observed to present a plateau, as SIC seemed to reach an equilibrium or a saturation point (Figure 9). Meanwhile, $\langle P_2^{RX} \rangle$ still increases above $\underline{CI_{norm}}$ = 0.7, reflecting those amorphous chains keep orienting. The sharp stress increase seems thus to originate from these chains, possibly reaching their full stretch conformation.

4. Conclusion

Hydrolysis was used to selectively modify the macromolecular structure a poly(ether-block-amide) copolymer (PEBA) and to investigate the strain-induced crystallization (SIC) contribution to the mechanical behaviour. Hydrolytic scissions were shown to predominantly occur at the ester function located between PA hard and PTMO soft segments, in the soft phase. This approach is particularly relevant, as scissions do not affect the PA crystalline domains, which was confirmed with static XRD analysis. It enables the behaviour of a range of PEBA samples presenting a given hard phase to be investigated, as they only differ by their soft phase macromolecular structure, that depends on their scission extend.

In situ XRD analysis combined with uniaxial testing enabled a remarkable correlation between stress and crystallinity to be highlighted, whatever the scission degree PEBA to which samples were subjected. This demonstrates that SIC is the driving phenomenon determining the PEBA stress response upon stretching. Consequently, with increasing scissions, the stress decrease observed at a given elongation can be fully interpreted as a consequence of a SIC weakening. Further tests, performed at different testing temperatures, confirmed this observation: even though the testing temperature and the chain scissions both significantly affect the SIC phenomenon and the PEBA mechanical properties, a strong correlation between stress and crystallinity is still observed. Overall, strain-induced crystallization is identified as a major phenomenon in understanding the mechanical behaviour of PEBA.

Corresponding Author

Pierre-Yves Le Gac

Marine Structure Laboratory, IFREMER, Centre de Bretagne, 29280 Plouzané, France

pierre.yves.le.gac@ifremer.fr

Funding Sources

We acknowledge the financial support provided by ANRT (CIFRE n°2016/0796).

Notes

The authors declare no competing financial interest.

Acknowledgements

We thank the SOLEIL synchrotron facility and the SWING beamline for access to the instrumentation and assistance during the WAXS and SAXS experiments. These experiments have been made during and in addition to the project n° 20170187. Sylvie Tencé-Girault (Arkema/PIMM laboratory) is sincerely thanked for her valuable help interpreting the XRD measurements and her global contribution to improve this article. The participation of Mathieu Gervais, Mickaël Premel-Cabic and Nicolas Lacotte is finally gratefully acknowledged.

References

[1] Trabelsi, S.; Albouy, P.-A.; Rault, J. Stress-Induced Crystallization around a Crack Tip in Natural Rubber. Macromolecules 2002, 35 (27), 10054–10061. https://doi.org/10.1021/ma021106c

[2] Trabelsi, S.; Albouy, P.-A.; Rault, J. Crystallization and Melting Processes in Vulcanized Stretched Natural Rubber. Macromolecules 2003, 36 (20), 7624–7639. https://doi.org/10.1021/ma030224c

[3] Imbernon, L.; Pauchet, R.; Pire, M.; Albouy, P.-A.; Tencé-Girault, S.; Norvez, S. Strain-Induced Crystallization in Sustainably Crosslinked Epoxidized Natural Rubber. Polymer 2016, 93, 189–197. https://doi.org/10.1016/j.polymer.2016.04.023

[4] Sotta, P.; Albouy, P.-A. Strain-Induced Crystallization in Natural Rubber: Flory's Theory Revisited. Macromolecules 2020, 53 (8), 3097–3109. https://doi.org/10.1021/acs.macromol.0c00515

[5] Albouy, P.-A.; Sotta, P. Draw Ratio at the Onset of Strain-Induced Crystallization in Cross-Linked Natural Rubber. Macromolecules 2020, 53 (3), 992–1000. https://doi.org/10.1021/acs.macromol.9b01957

[6] Le Gac, P.-Y.; Albouy, P.-A.; Petermann, D. Strain-Induced Crystallization in an Unfilled Polychloroprene Rubber: Kinetics and Mechanical Cycling. Polymer 2018, 142, 209–217. https://doi.org/10.1016/j.polymer.2018.03.034

[7] Le Gac, P.-Y.; Albouy, P.-A.; Sotta, P. Strain-Induced Crystallization in a Carbon-Black Filled Polychloroprene Rubber: Kinetics and Mechanical Cycling. Polymer 2019, 173, 158–165. https://doi.org/10.1016/j.polymer.2019.04.019

[8] Flory, P. J. Thermodynamics of Crystallization in High Polymers. I. Crystallization Induced by Stretching. J. Chem. Phys. 1947, 15 (6), 397–408. https://doi.org/10.1063/1.1746537

[9] Bonart, R. X-Ray Investigations Concerning the Physical Structure of Cross-Linking in Segmented Urethane Elastomers. Journal of Macromolecular Science, Part B 1968, 2 (1), 115–138. https://doi.org/10.1080/00222346808212867

[10] Xu, M.; MacKnight, W. J.; Chen-Tsai, C. H. Y.; Thomas, E. L. Structure and Morphology of Segmented Polyurethanes: 4. Domain Structures of Different Scales and the Composition Heterogeneity of the Polymers. Polymer 1987, 28 (13), 2183–2189. https://doi.org/10.1016/0032-3861(87)90373-9

[11] Reynolds, N.; Spiess, H. W.; Hayen, H.; Nefzger, H.; Eisenbach, C. D. Structure and Deformation Behaviour of Model Poly(Ether-Urethane) Elastomers, 1. Infrared Studies. Macromolecular Chemistry and Physics 1994, 195 (8), 2855–2873. https://doi.org/10.1002/macp.1994.021950816

[12] Mclean, R. S.; Sauer, B. B. Nano-Deformation of Crystalline Domains during Tensile Stretching Studied by Atomic Force Microscopy. Journal of Polymer Science Part B: Polymer Physics 1999, 37 (8), 859–866. https://doi.org/10.1002/(SICI)1099-0488(19990415)37:8<859::AID-POLB11>3.0.CO;2-U

[13] Armstrong, S.; Freeman, B.; Hiltner, A.; Baer, E. Gas Permeability of Melt-Processed Poly(Ether Block Amide) Copolymers and the Effects of Orientation. Polymer 2012, 53 (6), 1383–1392. https://doi.org/10.1016/j.polymer.2012.01.037

[14] Barbi, V.; Funari, S. S.; Gehrke, R.; Scharnagl, N.; Stribeck, N. SAXS and the Gas Transport in Polyether-Block-Polyamide Copolymer Membranes. Macromolecules 2003, 36 (3), 749–758. https://doi.org/10.1021/ma0213403

[15] Zhu, P.; Dong, X.; Wang, D. Strain-Induced Crystallization of Segmented Copolymers: Deviation from the Classic Deformation Mechanism. Macromolecules 2017, 50 (10), 3911–3921. https://doi.org/10.1021/acs.macromol.6b02747

[16] Hucher, C.; Eustache, R.-P.; Beaume, F.; Tekely, P. Motional Heterogeneity in Poly(Ether-Block-Amide) Copolymers As Revealed by Solid-State NMR. Macromolecules 2005, 38 (22), 9200–9209. https://doi.org/10.1021/ma051625q

[17] Sheth, J. P.; Xu, J.; Wilkes, G. L. Solid State Structure–Property Behavior of Semicrystalline Poly(Ether-Block-Amide) PEBAX® Thermoplastic Elastomers. Polymer 2003, 44 (3), 743–756. https://doi.org/10.1016/S0032-3861(02)00798-X

[18] Buckwalter, D. J.; Dennis, J. M.; Long, T. E. Amide-Containing Segmented Copolymers. Progress in Polymer Science 2015, 45, 1–22. https://doi.org/10.1016/j.progpolymsci.2014.11.003

[19] Song, Y.; Yamamoto, H.; Nemoto, N. Segmental Orientations and Deformation Mechanism of Poly(Ether-Block-Amide) Films. Macromolecules 2004, 37 (16), 6219–6226. https://doi.org/10.1021/ma0400620

[20] Sauer, B. B.; McLean, R. S.; Brill, D. J.; Londono, D. J. Morphology and Orientation during the Deformation of Segmented Elastomers Studied with Small-Angle X-Ray Scattering and Atomic Force Microscopy. J. Polym. Sci. B Polym. Phys. 2002, 40 (16), 1727–1740. https://doi.org/10.1002/polb.10234

[21] Bardin, A. Durability of Thermoplastic Elastomers for Marine Applications. PhD Manuscript, Paris, HESAM, 2020. https://pastel.archives-ouvertes.fr/tel-02948183

[22] Bardin, A.; Le Gac, P.-Y.; Cérantola, S.; Simon, G.; Bindi, H.; Fayolle, B. Hydrolytic Kinetic Model Predicting Embrittlement in Thermoplastic Elastomers. Polymer Degradation and Stability 2020, 171, 109002. https://doi.org/10.1016/j.polymdegradstab.2019.109002

[23] Bardin, A.; Gac, P.-Y. L.; Bindi, H.; Fayolle, B. Relationships between Molar Mass and Fracture Properties of Segmented Urethane and Amide Copolymers Modified by Chemical Degradation. Journal of Polymer Science 2020, 58 (22), 3170–3182. https://doi.org/10.1002/pol.20200460

[24] Wang, Y.; Zhu, P.; Lai, Y.; Wang, L.; Wang, D.; Dong X. Effect of crosslinking networks on strain-induced crystallization in polyamide 1012 multiblock Poly(tetramethylene oxide) copolymers Polymer 225 (2021) 123802. https://doi.org/10.1016/j.polymer.2021.123802

[25] Rezac, M. E.; John, T.; Pfromm, P. H. Effect of Copolymer Composition on the Solubility and Diffusivity of Water and Methanol in a Series of Polyether Amides. J. Appl. Polym. Sci. 1997, 65 (10), 1983–1993. https://doi.org/10.1002/(SICI)1097-4628(19970906)65:10<1983::AID-APP16>3.0.CO;2-Y

[26] Kaddour Djebbar, M.; Nguyen, Q. T.; Clément, R.; Germain, Y. Pervaporation of Aqueous Ester Solutions through Hydrophobic Poly(Ether-Block-Amide) Copolymer Membranes. Journal of Membrane Science 1998, 146 (1), 125–133. https://doi.org/10.1016/S0376-7388(98)00090-8

[27] Zhang, C.-L.; Feng, L.-F.; Gu, X.; Hoppe, S.; Hu, G.-H. Determination of the Molar Mass of Polyamide Block/Graft Copolymers by Size-Exclusion Chromatography at Room Temperature. Polymer Testing 2007, 26 (6), 793–802. https://doi.org/10.1016/j.polymertesting.2007.04.011

[28] Albouy, P.-A.; Guillier, G.; Petermann, D.; Vieyres, A.; Sanseau, O.; Sotta, P. A Stroboscopic X-Ray Apparatus for the Study of the Kinetics of Strain-Induced Crystallization in Natural Rubber. Polymer 2012, 53 (15), 3313–3324. https://doi.org/10.1016/j.polymer.2012.05.042

[29] Le Gac, P. Y.; Choqueuse, D.; Melot, D. Description and modeling of polyurethane hydrolysis used as thermal insulation in oil offshore conditions. Polymer Testing 2013, 32(8), 1588-1593. https://doi.org/10.1016/j.polymertesting.2013.10.009

[30] Yeol Lee, S.; Park, J. W.; Yoo, Y. T.; Im, S. S. Hydrolytic Degradation Behaviour and Microstructural Changes of Poly(Ester-Co-Amide)s. Polymer Degradation and Stability 2002, 78 (1), 63–71. https://doi.org/10.1016/S0141-3910(02)00120-9

[31] Deshayes, G.; Delcourt, C.; Verbruggen, I.; Trouillet-Fonti, L.; Touraud, F.; Fleury, E.; Degée, P.; Destarac, M.; Willem, R.; Dubois, P. Novel Polyesteramide-Based Di- and Triblock Copolymers: From Thermo-Mechanical Properties to Hydrolytic Degradation. European Polymer Journal 2011, 47 (1), 98–110. https://doi.org/10.1016/j.eurpolymj.2010.07.005

[32] Hatfield, G. R.; Guo, Y.; Killinger, W. E.; Andrejak, R. A.; Roubicek, P. M. Characterization of Structure and Morphology in Two Poly(Ether-Block-Amide) Copolymers. Macromolecules 1993, 26 (24), 6350–6353. https://doi.org/10.1021/ma00076a008

[33] Inoue, K.; Hoshino, S. Crystal Structure of Nylon 12. Journal of Polymer Science: Polymer Physics Edition 1973, 11 (6), 1077–1089. https://doi.org/10.1002/pol.1973.180110604

[34] Hiramatsu, N.; Haraguchi, K.; Hirakawa, S. Study of Transformations among α, γ and γ' Forms in Nylon 12 by X-Ray and DSC. JaJAP 1983, 22 (2), 335. https://doi.org/10.1143/JJAP.22.335

[35] Imada, K.; Miyakawa, T.; Chatani, Y.; Tadokoro, H.; Murahashi, S. Structural Studies of Polyethers, [-(CH2)m-O-]n. III1. Molecular and Crystal Structure of Polytetrahydrofuran. Die Makromolekulare Chemie 1965, 83 (1), 113–128. https://doi.org/10.1002/macp.1965.020830109

[36] Kamal, T.; Park, S.-Y.; Park, J.-H.; Chang, Y.-W. Structural Evolution of Poly(Ether-b-Amide12) Elastomers during the Uniaxial Stretching: An in Situ Wide-Angle X-Ray Scattering Study. Macromol. Res. 2012, 20 (7), 725–731. https://doi.org/10.1007/s13233-012-0109-z

[37] Le Gac, P. Y.; Albouy, P. A.; Fayolle, B.; Verdu, J. Relationship between macromolecular network and fatigue properties of unfilled polychloroprene rubber. Polymer Degradation and Stability 2021, 192, 109669. https://doi.org/10.1016/j.polymdegradstab.2021.109669

Highlights

* A range of PEBA presenting various macromolecular structures has been produced after hydrolysis
* Chain scission changes strain-induced crystallization (SIC) occurring during tensile loading
* A close correlation between stress and crystallinity induced under strain is highlighted

Declaration of interests

☒ The authors declare that they have no known competing financial interests or personal relationships that could have appeared to influence the work reported in this paper.

☐The authors declare the following financial interests/personal relationships which may be considered as potential competing interests: